



# 3D-printed ZSM-5 monoliths with metal dopants for methanol conversion in the presence and absence of carbon dioxide

Fatima Magzoub, Xin Li, Jawad Al-Darwish, Fateme Rezaei, Ali A. Rownaghi\*

Department of Chemical and Biochemical Engineering, Missouri University of Science and Technology, Rolla, MO, 65409, USA



## ARTICLE INFO

**Keywords:**  
3D printing  
ZSM-5 zeolite  
Doped metals  
CO<sub>2</sub> co-feeding  
MTH reaction

## ABSTRACT

The development of effective strategies to utilize CO<sub>2</sub> as a renewable feedstock for producing commercially-viable products is an interesting challenge to explore new concepts and opportunities in catalysis and industrial chemistry. In this study, 3D-printed ZSM-5 monoliths doped with Ga<sub>2</sub>O<sub>3</sub>, Cr<sub>2</sub>O<sub>3</sub>, CuO, ZnO, MoO<sub>3</sub>, and Y<sub>2</sub>O<sub>3</sub> were synthesized using the state-of-art 3D printing technique. The physicochemical properties of the catalysts were characterized by X-ray diffraction, N<sub>2</sub> physisorption, NH<sub>3</sub> and CO<sub>2</sub> temperature-programmed desorption and H<sub>2</sub> temperature-programmed reduction. The promotional effect of doped metals on catalytic performance of 3D-printed ZSM-5 monoliths in methanol to hydrocarbon (MTH) reaction in the presence and absence of CO<sub>2</sub> was investigated. Results indicated that both metal dopants type and reaction atmosphere greatly influence catalyst stability and product distribution. The yield of light olefins was enhanced over all metal-doped 3D-printed ZSM-5 monoliths in N<sub>2</sub> atmosphere (absence of CO<sub>2</sub>), however, CO<sub>2</sub> atmosphere did not favor the production of light olefins. Although selectivity toward ethylene slightly decreased, the propylene yield was almost constant after switching N<sub>2</sub> to CO<sub>2</sub> in MTH reaction at 400 °C. Furthermore, it was found that Y- and Zn-doped ZSM-5 monoliths exhibited higher yield of light olefins and BTX compounds in the in the absence and presence of CO<sub>2</sub>, respectively.

## 1. Introduction

The utilization of CO<sub>2</sub> as a sustainable carbon feedstock and soft oxidant for production of fuels and commercially value-added chemicals has drawn broad interests to the industrial chemistry [1–4]. Since CO<sub>2</sub> is a thermodynamically stable molecule, reactions of CO<sub>2</sub> must be combined with either high-energy reactants or use high temperature and pressure reaction conditions to gain a thermodynamic driving force. Several CO<sub>2</sub> utilization processes have been developed that lead to production of urea, methanol, and salicylic acid. Moreover, the promotional effects of CO<sub>2</sub> as a soft oxidant on alkane dehydrogenation (C–H bond scission) and cycloaddition over homogeneous and heterogeneous catalysts have been investigated in detail [5–9]. As well-established in the literature, CO<sub>2</sub> can stabilize the catalyst by eliminating coke through the reverse Boudouard reaction (CO<sub>2</sub> + C ⇌ 2CO;  $\Delta H_{298}^\circ = +172 \text{ kJ mol}^{-1}$ ) [10–12]. Among the investigated materials, zeolite-supported metal oxides that act as bifunctional catalysts offer promising performance in CO<sub>2</sub> capture and utilization through cooperative interactions between Brønsted/ Lewis acid sites on zeolite and active metal centers which lead to improved stability and selectivity [12].

The effects of CO<sub>2</sub> co-feeding on catalyst performance are not clear and researchers have yet to reach a consensus on the exact role of CO<sub>2</sub> in various utilization reactions. For instance, De Lima and co-workers added CO<sub>2</sub> as a co-feed to the ethanol steam reforming process and reported enhanced stability of Pt/CeO<sub>2</sub> catalyst and high selectivity towards hydrogen [13]. In another investigation, Díaz and co-workers studied the influence of CO<sub>2</sub> co-feeding on Fischer-Tropsch fuels production over carbon nanofibers supported cobalt catalyst and found that the presence of CO<sub>2</sub> favors the formation of lighter hydrocarbons [14]. Xu and co-workers developed metal modified ZSM-5 catalysts for the methanol to aromatics conversion (MTA) under the CO<sub>2</sub> flow. It was demonstrated that the catalysts doped with Zn, Ni, and Ag were capable of increasing the total aromatics yield in the CO<sub>2</sub> atmosphere [15].

Among heterogeneous catalysts studied for the methanol to hydrocarbons (MTH) reaction, HZSM-5 and SAPO-34 materials with a number of metal promoters such as Ga<sub>2</sub>O<sub>3</sub>, Cr<sub>2</sub>O<sub>3</sub>, CuO, ZnO, MoO<sub>3</sub>, and Y<sub>2</sub>O<sub>3</sub> are found to be the most efficient catalysts owing to their unique pore network, high chemical and thermal stability as well as bifunctional properties [16–21]. Literature shows that the catalytic behavior of HZSM-5 and SAPO-34 materials for chemical transformation reactions is highly dependent on catalyst synthesis conditions,

\* Corresponding author.

E-mail address: [rownaghia@mst.edu](mailto:rownaghia@mst.edu) (A.A. Rownaghi).

zeolite framework, and metal promoters [22].

For practical applications, the synthesized powder materials need to be formed into monoliths or pellets before utilization at chemical industry [23]. Zeolite monoliths are structured materials with parallel gas flow channels [24]. The shape, channel size, and textural (i.e. pore distribution and exposed surface) and structural properties (e.g. active phase and amorphization) could be fine-tuned and precisely controlled in monolithic catalysts. Previous studies have examined structure-property relationships of ZSM-5 monolith and their powder counterpart [25,26]. Ivanova et al. [27] reported higher activity and selectivity for ZSM-5@ $\beta$ -SiC monolith than those for catalyst powder prepared under the same synthesis conditions. Tao et al. [28] prepared a highly crystalline meso-ZSM-5 monolith that consisted of both micropores and mesopores by using a template of carbon aerogel to impart uniform mesoporosity to the zeolite. Beers et al. [29] coated H-BEA, H-FAU on a cordierite (2Al<sub>2</sub>O<sub>3</sub>·5SiO<sub>2</sub>·2MgO) monolithic substrate and the coated monoliths resulted in an active and selective integrated catalyst-reactor configuration for the acylation of aromatics.

Recently, additive manufacturing by 3D printing has gained worldwide attention in formulation of porous materials into practical contactors as a result of flexibility in design alteration and preparation of robust and complex geometries which requires fewer steps and minimal resources in comparison to the previously established extrusion process [30–32]. Most recently, a number of porous materials such as zeolites (ZSM-5, Y, SAPO-34), metal-organic frameworks (MOFs) and Cu/Al<sub>2</sub>O<sub>3</sub> monoliths have been fabricated by 3D printing and used for catalysis and gas separation applications [33–37]. For instance, Rezaei and co-workers developed 3D-printed porous materials such as zeolite 5A and 13X monoliths, MOFs, aminosilicates and polymer-zeolite composites and confirmed their adsorption efficacy for CO<sub>2</sub> capture processs [33–35,38,39]. Couck et al. [40,41] produced SAPO-34 zeolite based monolith with honeycomb shape and utilized in CO<sub>2</sub>/N<sub>2</sub> separation. Lefevere et al. studied the effect of binders on mechanical and acidity of 3D-printed ZSM-5 zeolite [36,37]. In our previous works [25,26,42,43], we synthesized hierarchical ZSM-5 zeolite monoliths with macro-meso-microporosity using the 3D printing technique. The 3D-printed monolithic catalysts exhibited a more stable activity in *n*-hexane cracking and higher selectivity to light olefins than their powder counterpart [25,26].

In consideration of improved catalytic performance over 3D-printed zeolite monoliths, the objective of this study was to develop monolithic catalysts comprising Ga<sub>2</sub>O<sub>3</sub>-, Cr<sub>2</sub>O<sub>3</sub>-, CuO-, ZnO-, and Y<sub>2</sub>O<sub>3</sub>-doped ZSM-5 and demonstrate their catalytic efficacy as bifunctional catalysts in MTH reaction with CO<sub>2</sub> co-feeding in order to establish a useful guideline for extrapolating, normalizing, and correlating between monolith catalyst properties and performance. The activity of the catalysts and the selectivity to light olefins and BTX (benzene, toluene, and xylene) were compared in the presence and absence of CO<sub>2</sub>.

## 2. Experimental section

### 2.1. Preparation of the 3D-printed monolith

ZSM-5 zeolite (SiO<sub>2</sub>/Al<sub>2</sub>O<sub>3</sub> mole ratio of 50) monoliths were synthesized from ammonia-ZSM-5 powder (CBV 5524 G, Zeolyst). The commercial zeolite powder was first calcined at 550 °C for 6 h to produce proton-form of ZSM-5. In the next step, approximately 87.5 wt.% calcined ZSM-5 powder was mixed with 10 wt.% bentonite clay binder (Sigma-Aldrich) using an agitator (Model IKA-R25). Sufficient deionized water was then added to the mixture until a homogeneous slurry was formed, followed by the addition of a plasticizer, methyl cellulose (Sigma-Aldrich), to generate an aqueous paste with extrudable viscosity under stir. The paste was filled into a 10 mL syringe (Techcon Systems) furnished with a 0.60 mm nozzle. The synthesis of the monolith was perform on a lab-scale 3D printer and the printing paths of which was designed by AutoCAD and coded by Slic3r in advance. The paste was

dispensed and deposited on an alumina substrate in a layer-by-layer manner to produce a honeycomb-like monolith. The 3D-printed monoliths were dried overnight and then calcined for 6 h at 600 °C to remove methyl cellulose. The cross sectional surface of the cylinder monolith possessed 50% infill density resulting in a 0.60 mm wall thickness. For the metal doped ZSM-5 monoliths, approximately 10 wt.% of metal in its nitrate form was added to the zeolite/bentonite mixture and rolled with grinding medium overnight to obtain a homogenous slurry. Metal dopants were added into the zeolite paste before printing, thus eliminating the additional step of ion-exchange or impregnation that are commonly used for doping zeolite catalysts. The precursors used were Cr(NO<sub>3</sub>)<sub>3</sub>·9H<sub>2</sub>O, Cu(NO<sub>3</sub>)<sub>2</sub>·2.5H<sub>2</sub>O, Ga(NO<sub>3</sub>)<sub>3</sub>·xH<sub>2</sub>O, Y(NO<sub>3</sub>)<sub>3</sub>·6H<sub>2</sub>O, and Zn(NO<sub>3</sub>)<sub>2</sub>·6H<sub>2</sub>O (Sigma-Aldrich). The rest of preparation steps were the same as the bare ZSM-5 monolith preparation steps.

### 2.2. Catalysts characterization

X-ray diffraction (XRD) analysis was performed on a PANalytical X'Pert multipurpose X-ray diffractometer in the angle (2θ) range of 5°–50° with Cu-Kα1 radiation (40 kV and 40 mA) at a rate of 2.0° min<sup>-1</sup>. Nitrogen physisorption measurements were performed on a Micromeritics 3Flex surface characterization analyzer at 77 K. Prior to the measurements, the samples were degassed at 300 °C in vacuum for 6 h. Total surface area was determined by the Brunauer-Emmett-Teller (BET) method using the relative pressure (P/P<sub>0</sub>) in the range of 0.05–0.3. The total pore volume was calculated at the P/P<sub>0</sub> = 0.99 whereas the micropore volume was estimated by t-plot methods. The bulk composition of the materials was determined using a Perkin-Elmer Emission Spectrometer Model Plasma 1000 inductively coupled plasma-atomic emission spectrometer (ICP-AES). The dispersion of doped metals of the 3D-printed monoliths was analyzed by energy dispersive X-ray spectrometry (EDX).

Temperature-programmed desorptions of ammonia and CO<sub>2</sub> (NH<sub>3</sub>-TPD, CO<sub>2</sub>-TPD) were carried out to investigate the acidic and basic properties of the metal-doped 3D-printed ZSM-5 monolith catalysts. Both NH<sub>3</sub> and CO<sub>2</sub> adsorptions were performed on the Micromeritics 3Flex analyzer under a flow of 5% NH<sub>3</sub>/He or CO<sub>2</sub>/He at 100 °C. The desorptions of NH<sub>3</sub> or CO<sub>2</sub> were measured from 100 to 600 °C at a constant ramp rate of 10 °C min<sup>-1</sup>. A mass spectroscopy (BELMass) was used to detect the quantity of desorbed NH<sub>3</sub> and CO<sub>2</sub>. Temperature-programmed reduction with hydrogen (H<sub>2</sub>-TPR) was performed from 50 to 850 °C under a flow of 5% H<sub>2</sub>/He using the same instrument. The functional groups of the catalysts were determined by the FTIR spectra, obtained on a Nicolet-FTIR Model 750 spectrometer. Thermogravimetric analysis-differential thermal analysis (TGA-DTA) of the spent catalysts was carried out from 30 to 900 °C using TGA (Model Q500, TA Instruments), at a rate of 10 °C min<sup>-1</sup> in a 60 mL min<sup>-1</sup> air flow.

### 2.3. MTH reaction

The catalytic performance of 3D-printed monoliths in methanol conversion reaction was evaluated in a down-flow fixed-bed reactor setup. Nitrogen flow saturated with methanol at 30 °C was fed into the stainless-steel reactor with an inner diameter of 10 mm. The feed flow rate was controlled by a mass flow controller (Brooks, 5850). In a typical run, 0.3 g of catalyst was tested under 400 °C at 1.01 bar with a weight hourly space velocity (WHSV) of 0.35 h<sup>-1</sup>. The catalyst was activated *in-situ* at 550 °C under nitrogen flow for 2 h. The products were directly transferred to an on-line gas chromatography (SRI 8610C) and analyzed every hour with a flame ionized detector (GC-FID) connected to mxt-wax/mxt-alumina capillary column. The inlet line to the reactor was kept heated at 110 °C, whereas the effluent line of the reactor until GC injector was kept at 145 °C to prevent potential condensation of hydrocarbons. For the reaction under CO<sub>2</sub> atmosphere, the

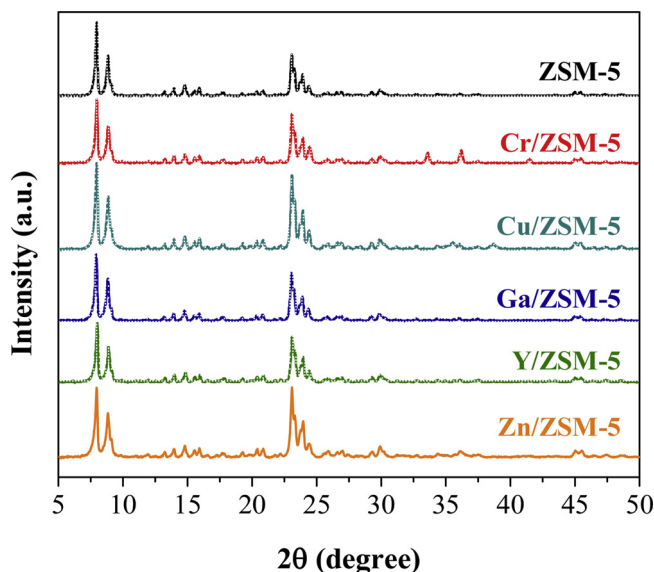


**Fig. 1.** XRD patterns of the bare and Cr, Cu, Ga, Y, and Zn-doped 3D-printed ZSM-5 monoliths.

nitrogen was substituted with  $\text{CO}_2$  while keeping other test conditions the same.

### 3. Results and discussion

#### 3.1. Characterization of the 3D-printed monoliths

The XRD patterns shown in **Fig. 1** indicate that structure and crystallinity of ZSM-5 zeolite were retained after printing for both pure ZSM-5 and doped-ZSM-5 monoliths with various metals. The peaks observed at  $2\theta = 8.0, 9.0, 14.8, 22.9, 24.0$  and  $29.8^\circ$ , were related to (101), (200), (301), (501), (303), and (503) planes, respectively, which verified the typical MFI structure [44]. For Cr/ZSM-5, the appearance of additional peaks at  $2\theta = 33.6^\circ, 36.1^\circ$  and  $41.5^\circ$  suggested the formation of  $\text{Cr}_2\text{O}_3$  [45]. Several peaks with less intensity were also observed at  $2\theta = 35.6^\circ$  and  $38.7^\circ$  for Cu/ZSM-5, and at  $2\theta = 36.2^\circ$  for Zn/ZSM-5, which indicated the formation of  $\text{CuO}$  and  $\text{ZnO}$ , respectively in these materials [15,46]. On the other hand, Ga/ZSM-5 and Y/ZSM-5 showed no observable peaks for their corresponding metal oxides. This might be due to the high dispersion of the oxides in the zeolite monoliths which made them difficult to detect by XRD beam [21,47].

The FTIR spectra of the investigated catalysts, shown in **Fig. 2**, provided another aspect to confirm the ZSM-5 structure of the 3D-printed monoliths. The peak at about  $450\text{ cm}^{-1}$  was ascribed to the vibration of internal Si-O or Al-O bonds of the  $\text{SiO}_4$  or  $\text{AlO}_4$  tetrahedra, whereas the peak observed at  $560\text{ cm}^{-1}$  was associated with external bonds of double five-member ring [48]. In addition, the peak at  $810\text{ cm}^{-1}$  was corresponded to symmetric stretching of external bonds between tetrahedral, whereas the strongest absorption peak appeared about  $1110\text{ cm}^{-1}$  was related to the internal asymmetric stretching of  $\text{Si}-\text{O}-\text{Si}(\text{Al})$  bonds [49]. An additional band observed at around  $1240\text{ cm}^{-1}$  was associated with the asymmetric stretching vibration of Al–O or Si–O bonds. The presence of these peaks clearly indicated that the catalysts retained their MFI structure after metal doping, in accordance with the XRD results, discussed earlier.

The Bands for hydroxyl groups ( $-\text{OH}$ ) were also detected in the range of  $4000\text{--}3200\text{ cm}^{-1}$ . The peak appeared at  $3745\text{ cm}^{-1}$  was related to the vibration of  $-\text{OH}$  groups connected to the silicon atom ( $\text{Si}-\text{OH}$ ), which were mostly on the external surface of the zeolite [50]. The bands observed at  $3665\text{--}3610\text{ cm}^{-1}$  were ascribed to the hydroxyl groups connected by Al–OH bonds. Specifically, the band at  $3655\text{ cm}^{-1}$  was associated with the external Al-bonded hydroxyl

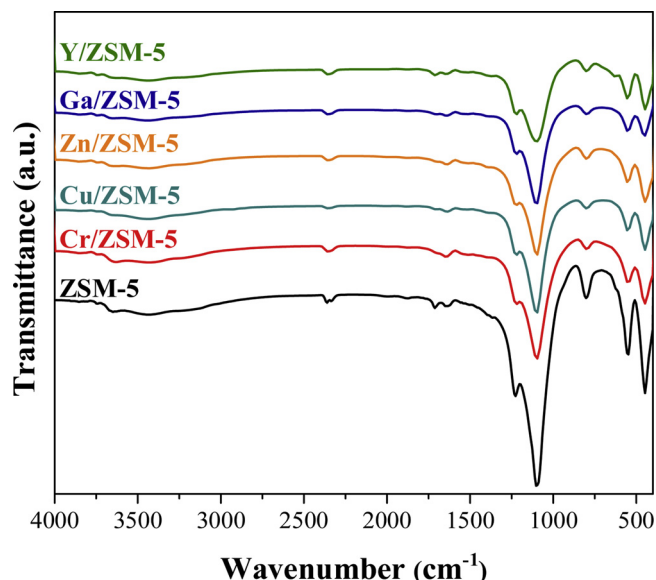


**Fig. 2.** FTIR spectra of the bare and Cr, Cu, Ga, Y, and Zn-doped 3D-printed ZSM-5 monoliths.

groups with weak Brønsted acidity while the band at  $3620\text{ cm}^{-1}$  was associated with the internal bridging hydroxyl groups ( $\text{Si}-\text{OH}-\text{Al}$ ) with strong Brønsted acidity [51]. For Cr/ZSM-5, Cu/ZSM-5 and Zn/ZSM-5 samples, the intensity of the bands in this range remained relatively high, indicating the intact hydroxyl groups but formation of metal oxide on zeolite surface.

The textural properties of the monolith catalysts determined by  $\text{N}_2$  physisorption measurements as well as the actual metal loading measured by elemental analysis (ICP-AES) are listed in **Table 1**. Due to the addition of binder and further calcination of fresh monoliths and decomposition of the plasticizer, the BET surface area of 3D-printed ZSM-5 monolith was reduced from  $429\text{ cm}^2\text{ g}^{-1}$  to  $373\text{ cm}^2\text{ g}^{-1}$ , while mesopore volume increased from  $0.170\text{ cm}^3\text{ g}^{-1}$  to  $0.200\text{ cm}^3\text{ g}^{-1}$ . Results of ICP-AES revealed that the actual metal contents were close to the nominal loading (10 wt%) and all metal-doped monoliths contained approximately 10 wt% metal. Furthermore, it was noticed that the metal dopants slightly decreased both the total surface area and the pore volume of the monoliths, which was close to the theoretical values added into the zeolite paste before printing. The change of the

**Table 1**

Surface area, pore volumes, and metal content of the 3D-printed ZSM-5 monoliths.

Sample	Surface area ( $\text{m}^2\text{ g}^{-1}$ ) <sup>a</sup>	Total Pore volume ( $\text{cm}^3\text{ g}^{-1}$ ) <sup>b</sup>	Micropore volume ( $\text{cm}^3\text{ g}^{-1}$ ) <sup>c</sup>	Mesopore volume ( $\text{cm}^3\text{ g}^{-1}$ ) <sup>c</sup>	Metal loading (wt%) <sup>d</sup>
ZSM-5(powder)	429	0.300	0.130	0.170	–
ZSM-5(monolith)	373	0.300	0.100	0.200	–
Cr/ZSM-5	286	0.219	0.090	0.129	10.6
Cu/ZSM-5	297	0.202	0.096	0.106	9.8
Ga/ZSM-5	318	0.213	0.096	0.117	10.0
Y/ZSM-5	293	0.208	0.090	0.118	10.3
Zn/ZSM-5	285	0.227	0.090	0.137	10.3

<sup>a</sup>  $S_{\text{BET}}$  was obtained by analyzing nitrogen adsorption data at  $-196^\circ\text{C}$  in a relative vapor pressure ranging from 0.05 to 0.30.

<sup>b</sup> Total pore volume was estimated based on the volume adsorbed at  $P/P_0 = 0.99$ .

<sup>c</sup> Micropore area and micropore volume were determined using t-plot method.

<sup>d</sup> The metal loading was measured by ICP.

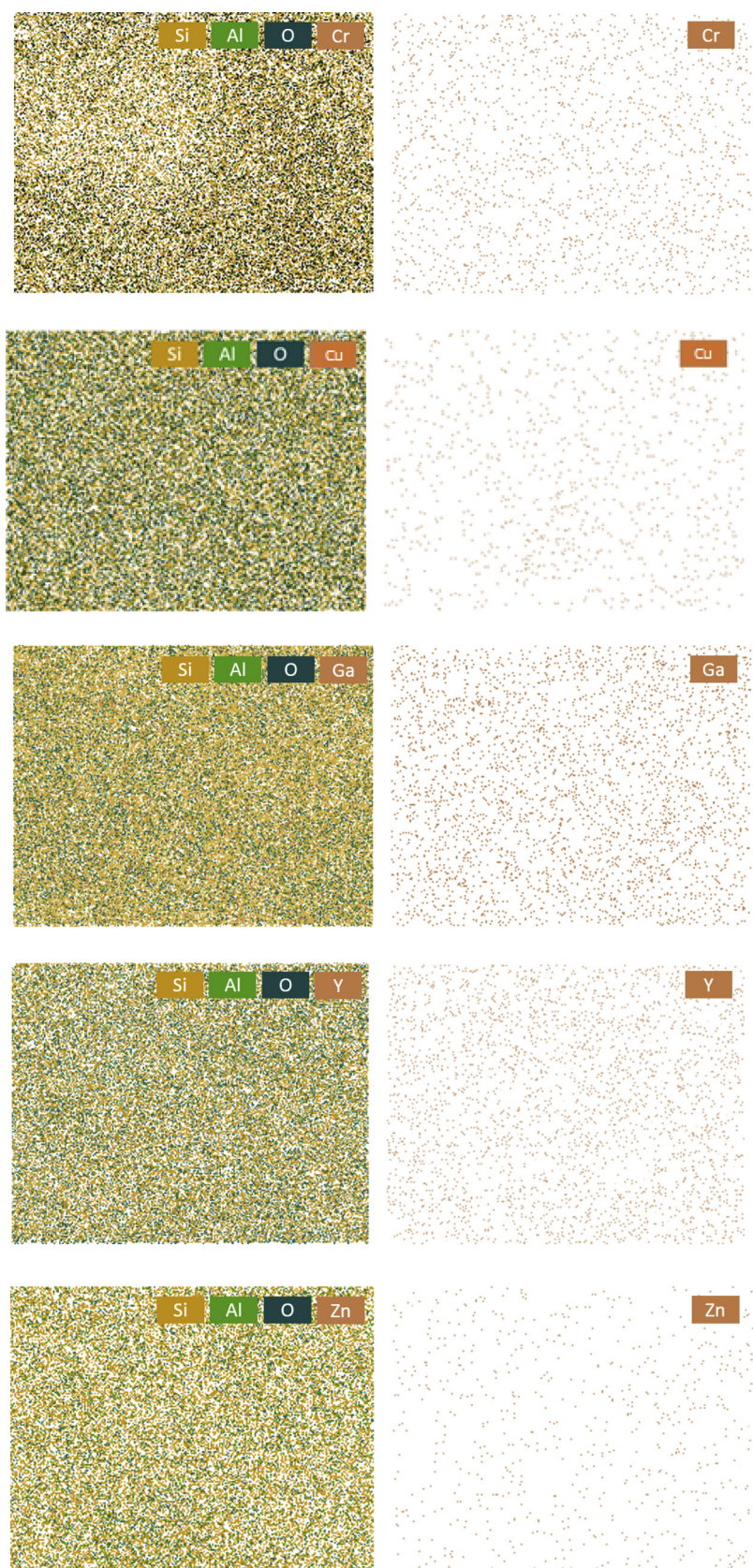


**Fig. 3.** EDX analysis and corresponding mapping of the elements in Cr/ZSM-5, Cu/ZSM-5, Ga/ZSM-5, Y/ZSM-5, and Zn/ZSM-5 monoliths.

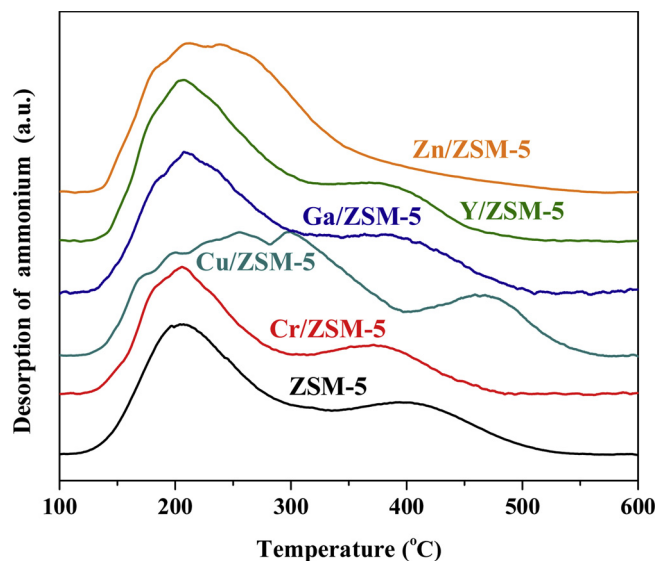


**Fig. 4.** NH<sub>3</sub>-TPD profiles of the bare and Cr-, Cu-, Ga-, Y-, and Zn-doped 3D-printed ZSM-5 monoliths.

micropore volume was less significant than the change in the mesopore volume after metal incorporation, suggesting that the decrease in pore volume resulted from the metal dopant clogging in the mesopores of the monolith.

The distribution of doped metals within the ZSM-5 monolith was investigated by elemental mapping. The successful incorporation of metal particles was further confirmed by the presence of corresponding metal, oxygen, Si and Al in the EDX patterns and element mappings (Fig. 3), which proved that the metal oxide nanoparticles were distributed homogeneously within the 3D-printed ZSM-5 monoliths.

The acidic properties of the 3D-printed monoliths were characterized by NH<sub>3</sub>-TPD and the results are shown in Fig. 4. All samples exhibited two desorption peaks at around 102 and 413 °C, which were due to the presence of the weak acid sites (Brønsted and/or Lewis sites) and strong Brønsted acid sites, respectively. As summarized in Table 2, metal loading slightly increased the surface acidity (number of acid sites and/or acid strength) of the metal doped-3D-printed monoliths except for Cr/ZSM-5 monoliths. It should be noted here that the Cr/ZSM-5 monolith displayed the same profile shape as the bare ZSM-5 monolith mainly because the chromium existed in its oxide form, as confirmed by XRD analysis. These results indicated that the acidity was barely affected by the chromium dopant. Moreover, for Cr-, Ga-, Y-, and Zn-doped 3D-printed ZSM-5 monoliths, the maximum of the peaks slightly shifted to the lower temperatures. The decrease of the second

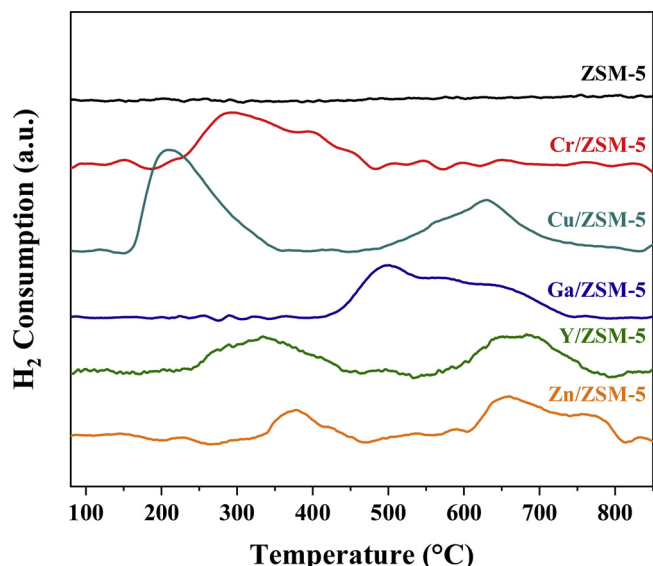


**Fig. 5.** H<sub>2</sub>-TPR profiles of the bare and Cr-, Cu-, Ga-, Y-, and Zn-doped 3D-printed ZSM-5 monoliths.

desorption peak was consistent with the high exchange degree of Brønsted acid sites in these samples leading to decrease in strong acid sites. A similar reduction in desorption temperature and density of strong acid sites was observed by Veses et al. [52] who prepared Ga-, Cu-, Sn-, and Ni-ZSM-5 catalysts.

For Cu/ZSM-5, the strength of acid sites was dramatically enhanced by the addition of copper, which is in consistent with previously reported work [52]. The ZSM-5 monoliths with Ga and Y dopants also exhibited similar TPD profiles to the bare ZSM-5 monolith, indicating that the addition of these metals to ZSM-5 had little effect on the acid strength, which might be due to the formation of micro metal oxide particles. In the case of Zn/ZSM-5, the second peak became less noticeable implying the reduced number of strong Brønsted acid sites, however, the total amount of weak acid sites, reflected by the peak area, was obviously increased, suggesting the zinc dopant converted the strong acid sites to the weak sites. This might be the result of the exchange of the proton on the hydroxyl group by Zn<sup>2+</sup>, or substitution interaction between Zn<sup>2+</sup> and protons of Si–OH-Al groups to form Zn(OH)<sup>+</sup> [53].

In order to study the reducibility of the various metal doped-3D-printed monoliths, H<sub>2</sub>-TPR analysis was performed, and the corresponding reduction curves and amount of H<sub>2</sub> consumption are shown in Fig. 5 and Table 2, respectively. According to the literature [12,22],

**Table 2**  
Summary of NH<sub>3</sub>-TPD and H<sub>2</sub>-TPR results.

Sample	H <sub>2</sub> reduction peak <sup>a</sup>		TPR peak area <sup>a</sup> (a.u.) × 10 <sup>-8</sup>	Weak acid peak <sup>b</sup>		Strong acid peak <sup>b</sup>		Total
	No.	T (°C)		T (°C)	Amount (mmol g <sup>-1</sup> )	T (°C)	Amount (mmol g <sup>-1</sup> )	
ZSM-5	–	–	–	210	0.4	394	0.16	0.56
Cr/ZSM-5	a	285	4.55	205	0.33	371	0.11	0.44
Cu/ZSM-5	a	206	5.67	297	0.56	459	0.15	0.72
	b	625	4.25					
Ga/ZSM-5	a	501	8.33	207	0.46	364	0.12	0.58
Y/ZSM-5	a	331	2.72	208	0.52	385	0.07	0.59
	b	686	2.68					
Zn/ZSM-5	a	376	0.96	208	0.54	375	0.06	0.6
	b	657	2.53					
	c	761	0.76					

<sup>a</sup> Obtained from H<sub>2</sub>-TPR results.

<sup>b</sup> Obtained from NH<sub>3</sub>-TPD results.

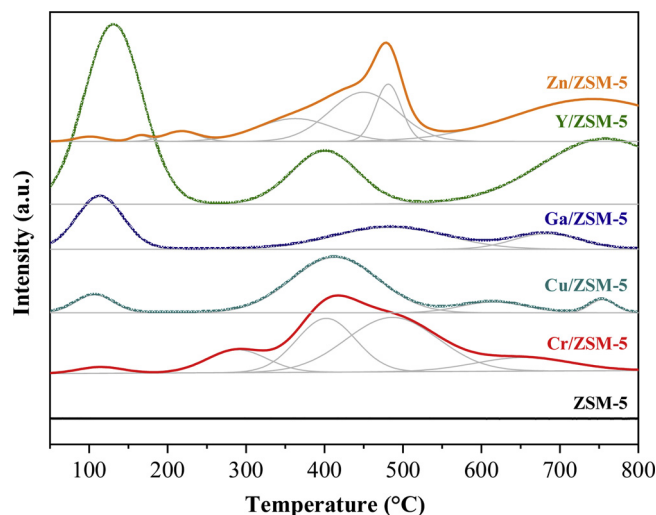


Fig. 6.  $\text{CO}_2$ -TPD profiles of the bare and Cr-, Cu-, Ga-, Y-, and Zn-doped 3D-printed ZSM-5 monoliths.

different reducibility of the metal oxides in the zeolite monolith is reflected by various peak positions. Metal-doped ZSM-5 monoliths displayed two reduction peaks which could be the result of two reduction steps for metal species. Cr/ZSM-5 exhibited a broad peak ranging from 250 to 450 °C, reflecting the reduction of  $\text{Cr}_2\text{O}_3$  to Cr, in agreement with the XRD result of  $\text{Cr}_2\text{O}_3$  presence [45]. For Cu/ZSM-5, the peaks observed at 207 and 627 °C were correlated to the reduction of dispersed bulk  $\text{CuO}$  and  $\text{Cu}^{2+}$  cations on the zeolite, respectively [15]. The latter form of metal needs more energy to be reduced than the former form. Similarly, two reduction peaks at around 503 and 617 °C were found for Ga/ZSM-5. They were associated with the micro  $\text{Ga}_2\text{O}_3$  particles and highly dispersed  $\text{GaO}^+$ , respectively [54]. This is in accordance with the XRD results for Ga/ZSM-5 that no  $\text{Ga}_2\text{O}_3$  peaks were found. For Y/ZSM-5, the peaks at 337 and 677 °C were ascribed to micro  $\text{Y}_2\text{O}_3$  particles and yttrium cations on zeolite, respectively, whereas the peaks at 377 and 657 °C for Zn/ZSM-5 can be assigned to  $\text{ZnO}$  and zinc cations, respectively.

To analyze the strength of the basic sites of Cr-, Cu-, Ga-, Y-, and Zn-doped 3D-printed ZSM-5 monolith catalysts, the  $\text{CO}_2$ -TPD experiments were conducted and the profiles are shown in Fig. 6. The characteristic peaks and their corresponding desorption temperature, which are indicative of amount of base sites (basicity) and base strength in the monoliths are also summarized in Table 3. It was revealed that total basicity of monoliths decreased in the order of Zn/ZSM-5 > Y/ZSM-5 > Cr/ZSM-5 > Cu/ZSM-5 > Ga/ZSM-5 > ZSM-5, which are in good agreement with adsorption of  $\text{CO}_2$  over Lewis acidic sites of metal

oxides. Basic properties of the materials depends upon the temperature profile in weak (< 200 °C), moderate (200–450 °C), and strong range (> 450 °C), respectively. As expected, no  $\text{CO}_2$  desorption peak was observed in the spectrum of bare ZSM-5 monolith, whereas the appearance of the desorption peaks in the spectra of metal doped-ZSM-5 monoliths demonstrated the interactions between the doped metals and  $\text{CO}_2$  molecules and that the enhancement of the basicity of the doped samples.

As Fig. 6 shows, all metal-doped ZSM-5 monoliths displayed first desorption peak in the range of 100–200 °C, which implied that they contained predominantly weak basic sites. In particular, Y/ZSM-5 and Ga/ZSM-5 monoliths exhibited high-intense peaks in this temperature range, indicating that the loading of Y and Ga only increased the number of weak adsorption active sites and did not enhance the overall adsorption strength. The weak adsorption of  $\text{CO}_2$  over Y/ZSM-5 and Ga/ZSM-5 monoliths limits its contact with the catalyst sites and thus weakens the consumption of hydrogen, which could increase the aromatics yield. The  $\text{CO}_2$  desorption peaks for Cr-, Cu-, and Zn-doped ZSM-5 monoliths were shifted to higher temperature, indicating strong interaction of the catalytic active sites with  $\text{CO}_2$ . The higher amount of moderate and strong active sites can activate the adsorbed  $\text{CO}_2$  to react with hydrogen in the reactor, thus enhance the yield of the aromatic hydrocarbons consequently [15].

### 3.2. MTH reaction in the presence and absence of $\text{CO}_2$

Methanol conversion was carried out at 400 °C and atmospheric pressure over bare and Cr-, Cu-, Ga-, Y-, and Zn-doped 3D-printed ZSM-5 monoliths. To probe the advantages of 3D-printed ZSM-5 monolith over its powder counterpart, a control experiment was performed in which the ZSM-5 powder and the bentonite clay (binder) with the same ratio as in the monolith were physically mixed and the reaction progress over it was monitored. As shown in Fig. 7a, it was observed that the methanol conversions were of the same at the beginning of the reaction, however, the methanol conversion decreased over time from about 95 to 90% over powder catalyst due to the carbon formation and deactivation. Since the composition (ratio of the zeolite/clay) in these two forms was the same, the better performance of the monolith catalyst could be thus correlated to its 3D-printed monolith structure. Fig. 7 illustrates  $\text{CH}_3\text{OH}$  conversion in the presence and absence of  $\text{CO}_2$  as a function of time-on-stream over the investigated monolith catalysts as well as the  $\text{CO}_2$  conversion in the  $\text{CO}_2$  atmosphere. It is evident that all monolith catalysts exhibited higher methanol conversion in the absence of  $\text{CO}_2$  (under  $\text{N}_2$  atmosphere). The trend for  $\text{CO}_2$  conversion was more stable than methanol conversion over all the monolith under the same condition. The conversion  $\text{CO}_2$  was less than 10% over the bare ZSM-5 (both powder and monolith) and Ga/ZSM-5 monoliths and remained constant over the time-on-stream. Among all the 3D-printed monoliths,

Table 3  
Summary of  $\text{CO}_2$ -TPD results.

Peak #	Sample	ZSM-5	Cr/ZSM-5	Cu/ZSM-5	Ga/ZSM-5	Y/ZSM-5	Zn/ZSM-5
1	T (°C)	–	114	107	114	131	101
	Peak area (mmol/g)	–	0.012	0.027	0.099	0.425	0.006
2	T (°C)	–	289	413	484	401	165
	Peak area (mmol/g)	–	0.055	0.194	0.099	0.142	0.004
3	T (°C)	–	402	615	683	759	217
	Peak area (mmol/g)	–	0.128	0.029	0.042	0.337	0.014
4	T (°C)	–	486	754	–	–	481
	Peak area (mmol/g)	–	0.203	0.013	–	–	0.060
5	T (°C)	–	653	–	–	–	363
	Peak area (mmol/g)	–	0.053	–	–	–	0.072
6	T (°C)	–	–	–	–	–	450
	Peak area (mmol/g)	–	–	–	–	–	0.137
7	T (°C)	–	–	–	–	–	742
	Peak area (mmol/g)	–	–	–	–	–	0.271

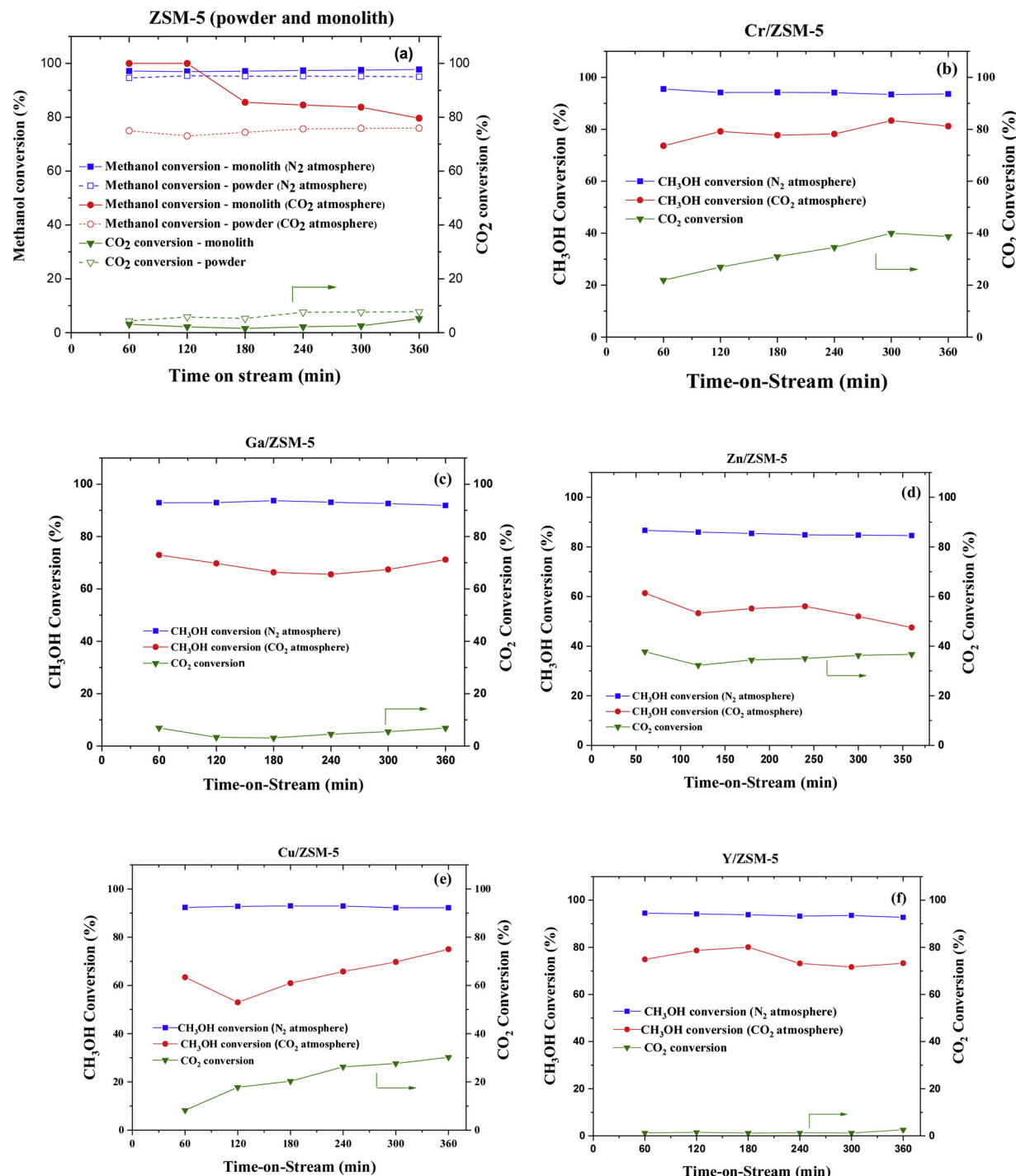


Fig. 7. Methanol conversion under N<sub>2</sub> and CO<sub>2</sub> atmospheres and CO<sub>2</sub> conversion in the presence and absence of CO<sub>2</sub> as a function of time-on-stream. Reaction temperature = 400 °C, WHSV = 0.35 h<sup>-1</sup>.

Y/ZSM-5 monolith resulted the lowest CO<sub>2</sub> conversion due to high density of weakly basic sites providing for low interaction of yttrium oxide with CO<sub>2</sub>. As for the Y/ZSM-5 monolith, the conversion of both methanol and CO<sub>2</sub> in the presence of CO<sub>2</sub> was more stable than those over other monoliths. The methanol conversions were about 95 and 75% within 360 min in the absence and presence of CO<sub>2</sub>, respectively. According to the H<sub>2</sub>-TPR profiles, yttrium oxide was present in both metal and cation forms, which exchanged the H<sup>+</sup> in the zeolite framework, as the latter peak indicated. From Table 2, there were less strong acid sites and more weak acid sites on Y/ZSM-5 than on the bare ZSM-5. Therefore, a combination of high density of weakly basic sites of

the doped metals and ZSM-5 catalytic function itself selectively decomposes methanol and enhances the formation of light olefins. As evident from N<sub>2</sub> physisorption results, the altered porosity might also be a factor that affects the activity.

Notably, the Cr/ZSM-5 monolith exhibited the highest selectivity to propylene with the highest CO<sub>2</sub> conversion (20–40%). Previous research has shown that in the presence of CO<sub>2</sub>, Cr<sup>3+</sup> and Cr<sup>2+</sup> sites participate additionally in an alternative oxidative pathway for propylene formation [12]. The methanol conversion over Cu/ZSM-5 monolith experienced a sharp decrease at 120 min followed by an increasing trend within 360 min from 50 to 78%. The maximum methanol

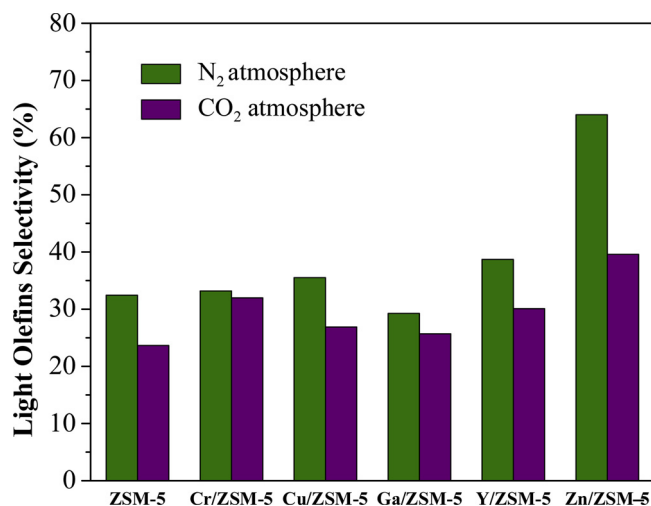


Fig. 8. Light olefins selectivity over the 3D-printed monoliths with various dopants in the presence and absence of CO<sub>2</sub>. Reaction temperature = 400 °C, WHSV = 0.35 h<sup>-1</sup>, product samples were tested for 120 min.

conversion was achieved for Y/ZSM-5 in the presence and absence of CO<sub>2</sub> within this series of monolith catalysts. Moreover, bare and metal-doped 3D printed ZSM-5 monoliths show more than 90% methanol conversion due to the relatively same density of acid sites. Linking both methanol and CO<sub>2</sub> conversion with the NH<sub>3</sub>-TPD and CO<sub>2</sub>-TPD profiles, it can be concluded that high population of moderate surface base sites in Cr/ZSM-5, Cu/ZSM-5, and Zn/ZSM-5 monoliths were responsible for catalyst stability in the presence of CO<sub>2</sub>.

As the major hydrocarbon products in methanol conversion processes, especially emphasized in MTH reaction, light olefins (i.e. ethylene, propylene, and butylene) are always considered. Fig. 8 shows the selectivity towards light olefins over 3D-printed monoliths under two different atmospheres. As shown in Fig. 8 and Table 4, the light olefins selectivity has been reduced over all 3D-printed ZSM-5 monoliths in the presence of CO<sub>2</sub>, nevertheless, the catalyst stability improved due to reverse Boudouard reaction, which prevents deposition of active carbon species on the metal surface. Moreover, this could be due to the difference in the particle size, reducibility of metals and surface texture of the metal oxides. From the detailed hydrocarbon product distribution data shown in Table 4, it can be noted that the reduction in the light olefins are mainly ethylene. Generally, the acidity increases the number of sites responsible for adsorption and polymerization of olefins [2]. These results indicate that the CO<sub>2</sub> co-feeding promotes cracking and dehydrocyclization, leading to production of light alkanes (methane and ethane) and BTX compounds.

Fig. 9 shows the effect of CO<sub>2</sub> co-feeding on BTX selectivity over 3D-

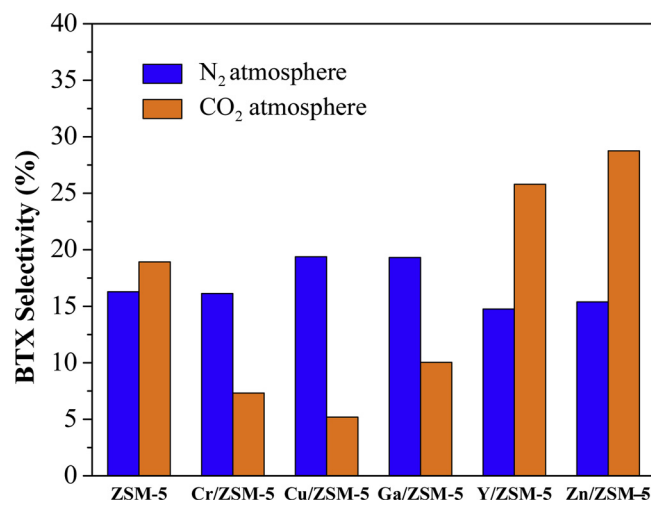


Fig. 9. BTX selectivity over the 3D-printed monoliths with various dopants in the presence and absence of CO<sub>2</sub>. Reaction temperature, 400 °C, WHSV = 0.35 h<sup>-1</sup>, product samples were tested for 120 min.

printed monoliths in MTH reaction. The product distribution for methanol conversion over bare and metal doped-ZSM-5 monolith catalysts in the presence and absence of CO<sub>2</sub> are summarized in Table 4. As evident from these results, the effect of CO<sub>2</sub> on BTX selectivity varied with the type of doped metal. For instance, although the selectivity towards BTX were significantly reduced over Cr/ZSM-5, Cu/ZSM-5, and Ga/ZSM-5 monolith catalysts in the presence of CO<sub>2</sub>, CO<sub>2</sub> co-feeding favored the formation of BTX over Y/ZSM-5 and Zn/ZSM-5 monoliths. The BTX selectivity over Y/ZSM-5 and Zn/ZSM-5 reached 26 and 29%, respectively. It indicated that the ZSM-5 catalysts modified with these two metals can catalyze the reaction of CO<sub>2</sub> with H<sub>2</sub>, which was generated in the methanol conversion, thereby consuming hydrogen atoms and reducing the formation of alkanes, as shown in Table 4, thus improving the yield of BTX [15]. The catalytic results also suggested that higher weak surface acidity and lower strong surface acidity favored ethylene and propylene production, whereas presence of CO<sub>2</sub> led to the production of more ethane. Thus the weak to moderate surface acid density are optimum for the selective conversion of methanol to propylene in the presence of CO<sub>2</sub>. Furthermore, the effect of metal doping on BTX selectivity was not significant in the absence of CO<sub>2</sub>, however, the ratio for benzene, toluene, and xylene dependent on the metal dopants. The BTX selectivities over Cu/ZSM-5 and Ga/ZSM-5 were slightly higher than the bare ZSM-5 monolith in the presence and absence of CO<sub>2</sub> which could be due to the dehydrogenation ability of these two metals that promoted the aromatization reaction [55,56].

The effect of surface acidity on the performance of zeolites in the

Table 4

Product distribution of methanol conversion over the 3D-printed monoliths (reaction temperature = 400 °C; WHSV = 0.35 h<sup>-1</sup>, product samples were tested for 120 min).

atmosphere	ZSM-5		Cr/ZSM-5		Cu/ZSM-5		Ga/ZSM-5		Y/ZSM-5		Zn/ZSM-5	
	N <sub>2</sub>	CO <sub>2</sub>										
Methane	1	4.1	1	11	2	15	2.6	8.8	2	6.2	6	5.5
Ethane	0	8.1	0	9	0	14	0.9	8.5	0	10	1	12
Ethylene	12	1	12	3.5	12	2.9	11	2.2	13	3.8	25	6
Propane	9	7	6	8.8	6	7.1	7.6	7.1	8	7.1	2	1.3
Propylene	14	10	17	20	14	16	12	10	16	12	28	25
Butane	17	9.7	15	15	13	11	15	11	14	7.4	2	3.8
Butylene	7	5.2	4	7.2	9	7.8	6.3	6.1	9	7.7	11	12
Benzene	2	3.8	8	1.5	8	2.9	8.3	4.3	8	4.1	3	4
Toluene	9	15	4	0.7	3	0.9	2.5	16	2	13	4	3.3
Xylene	5	15	3	4	8	2.7	8.5	3.5	5	8.4	8	11
others	25	21	28	20	24	19	25	22	23	20	10	16

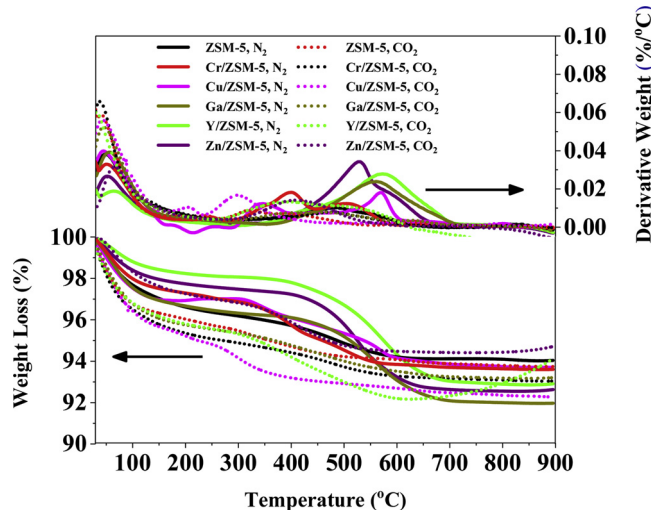


**Fig. 10.** TGA (lower) and DTA (upper) profiles of the spent catalysts after 6 h of methanol conversion at 400 °C in the presence and absence of CO<sub>2</sub>.

MTH reaction has been investigated by several research groups [57–59]. The incorporation of metal into the ZSM-5 paste enhanced the surface basicity while decreased the surface area of zeolite catalysts due to pore blockages by metal precursors. The obtained catalytic results demonstrated that metal doping enhances the catalyst stability in the absence of CO<sub>2</sub> due to decrease in the strong acid sites, which led to the suppression of the side reactions such as oligomerization and aromatization. Moreover, as shown in Table 3 and Fig. 7, with increasing the surface basicity, the activity of catalyst was enhanced in the presence of CO<sub>2</sub>.

Fig. 10 shows the amount of carbonaceous deposits on the bare and Cr-, Cu-, Ga-, Y-, and Zn-doped 3D-printed ZSM-5 monoliths after methanol conversion at 400 °C for 6 h time-on-stream in N<sub>2</sub> and CO<sub>2</sub> atmospheres. In general, the amount of carbonaceous products deposited in the presence of CO<sub>2</sub> was significantly lower than that in N<sub>2</sub> atmosphere over the same monoliths. All samples experienced a weight loss at around 100 °C, which was assigned to the moisture in the samples. Among all 3D-printed ZSM-5 monoliths, the amount of carbonaceous deposition was highest on Y/ZSM-5 and lowest over Cu/ZSM-5. Compared with the bare 3D-printed ZSM-5 monolith, although metal-doped 3D-printed ZSM-5 monoliths exhibited high selectivity toward light olefins and BTX compounds, they were rapidly deactivated due to coke deposition, which completely blocked the internal channels of the monoliths in the absence of CO<sub>2</sub>. On the contrary, the amount of coke deposited on all metal-doped 3D-printed ZSM-5 monoliths (except Zn/ZSM-5) was lower than on the bare ZSM-5 in the presence of CO<sub>2</sub> mainly due to reverse Boudouard reaction which can improve the catalyst stability. As shown in Table 2, Zn-doped 3D-printed ZSM-5 monolith gave rise to higher amount of propylene in the presence of CO<sub>2</sub>, which is the precursor for further carbon deposition.

#### 4. Conclusion

Herein, we reported the preparation ZSM-5 zeolite monoliths with various metal dopants using 3D printing technique. The metal dopants were added directly to the zeolite paste before printing. The catalytic behavior of these novel materials was evaluated in methanol conversion reaction under N<sub>2</sub> and CO<sub>2</sub> atmosphere. Characterization results of the catalysts suggested that the physiochemical properties of the ZSM-5 were modified by incorporation of metal dopants. The catalytic results indicated that the product distribution varied with the type of metal doped, and that methanol conversion was influenced by the acidity and basicity of the monoliths catalyst in the presence of CO<sub>2</sub>. Combined CO<sub>2</sub>-TPD, NH<sub>3</sub>-TPD, and catalytic evaluation results demonstrated that

the metal-doped ZSM-5 monolith possessed more weak to moderate acid and basic sites, which accounted for its superior catalytic performance. Unlike the lower ethylene yield, the amount of propylene and BTX compounds were enhanced in the presence of CO<sub>2</sub> over all metal-doped monoliths.

#### Funding

The authors declare no competing financial interest.

#### Acknowledgments

We thank the University of Missouri Research Board (UMRB) and Materials Research Center (MRC) of Missouri S&T for financially supporting this work.

#### References

- [1] K. Mondal, S. Sasmal, S. Badgandi, D.R. Chowdhury, V. Nair, Environ. Sci. Pollut. Res. 23 (2016) 22267–22273.
- [2] Q. Zhu, M. Takiguchi, T. Setoyama, T. Yokoi, J.N. Kondo, T. Tatsumi, Catal. Lett. 141 (2011) 670–677.
- [3] S. Fujita, M. Arai, B.M. Bhanage, Green Chemistry and Sustainable Technology, Springer, 2014.
- [4] A. Al-Mamoori, A. Krishnamurthy, A.A. Rownaghi, F. Rezaei, Energy Technol. 5 (2017) 834–849.
- [5] C. Häggström, O. Öhrman, A.A. Rownaghi, J. Hedlund, R. Gebart, Fuel Process. Technol. 94 (2012) 10–15.
- [6] H.Y. Chen, S.P. Lau, L. Chen, J. Lin, C.H.A. Huan, K.L. Tan, J.S. Pan, Appl. Surf. Sci. 152 (1999) 193–199.
- [7] A. Al-Mamoori, H. Thakkar, X. Li, A.A. Rownaghi, F. Rezaei, Ind. Eng. Chem. Res. 56 (2017) 8292–8300.
- [8] A. Jawad, F. Rezaei, A.A. Rownaghi, J. CO<sub>2</sub> Util. 21 (2017) 589–596.
- [9] X. Meng, H. He, Y. Nie, X. Zhang, S. Zhang, J. Wang, ACS Sustain. Chem. Eng. 5 (2017) 3081–3086.
- [10] T.C. Da Silva, J.F. Pinto, F.M. Santos, L.T. Dos Santos, D.A.G. Aranda, F. Ribeiro, N. Batalha, M.M. Pereira, Appl. Catal. B Environ. 164 (2015) 225–233.
- [11] T. Osaki, Catal. Lett. 145 (2015) 1931–1940.
- [12] M.A. Atanga, F. Rezaei, A. Jawad, M. Fitch, A.A. Rownaghi, Appl. Catal. B Environ. 220 (2018) 429–445.
- [13] S.M. De Lima, M. Adriana, G. Jacobs, B.H. Davis, L.V. Mattos, F.B. Noronha, Appl. Catal. B Environ. 96 (2010) 387–398.
- [14] J. Antonio, A. Raquel, D. Osa, P. Sánchez, A. Romero, J. Luis, Catal. Commun. 44 (2014) 57–61.
- [15] C. Xu, B. Jiang, Z. Liao, J. Wang, Z. Huang, Y. Yang, RSC Adv. 7 (2017) 10729–10736.
- [16] U.V. Mentzel, A.K. Rovik, C.H. Christensen, Catal. Lett. 127 (2009) 44–48.
- [17] A.A. Rownaghi, J. Hedlund, Ind. Eng. Chem. Res. 50 (2011) 11872–11878.
- [18] D. Freeman, R.P.K. Wells, G.H. Hutchings, Chem. Commun. 82 (2001) 1754–1755.
- [19] F.S.R. Barbosa, V.S.O. Ruiz, J.L.F. Monteiro, R.R. De Avillez, L.E.P. Borges, L.G. Appel, Catal. Lett. 126 (2008) 173–178.
- [20] Q. Yan, P.T. Doan, H. Toghiani, A.C. Gujar, M.G. White, J. Phys. Chem. C 112 (2008) 11847–11858.
- [21] A. Hwang, A. Bhan, ACS Catal. 7 (2017) 4417–4422.
- [22] X. Li, A. Kant, Y. He, H.V. Thakkar, M.A. Atanga, F. Rezaei, D.K. Ludlow, A.A. Rownaghi, Catal. Today 276 (2016) 62–77.
- [23] F. Rezaei, P. Webley, Chem. Eng. Sci. 64 (2009) 5182–5191.
- [24] F. Rezaei, P.A. Webley, Chem. Eng. Sci. 69 (2012) 270–278.
- [25] X. Li, W. Li, F. Rezaei, A. Rownaghi, Chem. Eng. J. 333 (2018) 545–553.
- [26] X. Li, A. Alwakwak, F. Rezaei, A.A. Rownaghi, ACS Appl. Energy Mater. 1 (2018) 2740–2748.
- [27] S. Ivanova, B. Louis, B. Madani, J.P. Tessonner, M.J. Ledoux, C. Pham-Huu, J. Phys. Chem. C 111 (2007) 4368–4374.
- [28] Y. Tao, H. Kanoh, K. Kaneko, J. Am. Chem. Soc. 125 (2003) 6044–6045.
- [29] A.E.W. Beers, T.A. Nijhuis, F. Kapteijn, J.A. Moulijn, Microporous Mesoporous Mater. 48 (2001) 279–284.
- [30] S. Mitchell, N. Michels, K. Kunze, J. Pe, Nat. Chem. 4 (2012) 825–831.
- [31] J. Freiding, B. Kraushaar-czarnetzki, Appl. Catal. A Gen. 391 (2011) 254–260.
- [32] J.L. Williams, Catal. Today 69 (2001) 3–9.
- [33] H. Thakkar, S. Eastman, A. Al-Mamoori, A. Hajari, A.A. Rownaghi, F. Rezaei, ACS Appl. Mater. Interfaces 9 (2017) 7489–7498.
- [34] H. Thakkar, S. Lawson, A.A. Rownaghi, F. Rezaei, Chem. Eng. J. 348 (2018) 109–116.
- [35] H. Thakkar, S. Eastman, Q. Al-Naddaf, A.A. Rownaghi, F. Rezaei, ACS Appl. Mater. Interfaces 9 (2017) 35908–35916.
- [36] J. Lefevere, S. Mullens, V. Meynen, Chem. Eng. J. 349 (2018) 260–268.
- [37] J. Lefevere, L. Protasova, S. Mullens, V. Meynen, Mater. Des. 134 (2017) 331–341.
- [38] H.V. Thakkar, S. Eastman, A. Hajari, A.A. Rownaghi, J.C. Knox, F. Rezaei, ACS Appl. Mater. Interfaces 8 (2016) 27753–27761.
- [39] S. Lawson, Q. Al-naddaf, A. Krishnamurthy, M.S. Amour, C. Griffin, A.A. Rownaghi,

J.C. Knox, F. Rezaei, *ACS Appl. Mater. Interfaces* 10 (2018) 19076–19086.

[40] S. Couck, J. Cousin-Saint-Remi, S. Van der Perre, G.V. Baron, C. Minas, P. Ruch, J.F.M. Denayer, *Microporous Mesoporous Mater.* 255 (2018) 185–191.

[41] S. Couck, J. Lefevere, S. Mullens, L. Protasova, V. Meynen, G. Desmet, G.V. Baron, J.F.M. Denayer, *Chem. Eng. J.* 308 (2017) 719–726.

[42] X. Li, F. Rezaei, A. Rownaghi, *Microporous Mesoporous Mater.* 276 (2019) 1–12.

[43] X. Li, F. Rezaei, A.A. Rownaghi, *React. Chem. Eng.* 3 (2018) 733–746.

[44] X. Li, F. Rezaei, D.K. Ludlow, A.A. Rownaghi, *Ind. Eng. Chem. Res.* 57 (2018) 1446–1453.

[45] N. Mimura, M. Okamoto, H. Yamashita, S.T. Oyama, K. Murata, *J. Phys. Chem. B* 110 (2006) 21764–21770.

[46] J. Ereña, J.M. Arandes, J. Bilbao, A.T. Aguayo, H.I. de Lasa, *Ind. Eng. Chem. Res.* 37 (1998) 1211–1219.

[47] D. Freeman, R.P.K. Wells, G.J. Hutchings, *J. Catal.* 205 (2002) 358–365.

[48] J.C. Jansen, F.J. van der Gaag, H. van Bekkum, *Zeolites* 4 (1984) 369–372.

[49] I.C.L. Barros, V.S. Braga, D.S. Pinto, J.L. de Macedo, G.N.R. Filho, J.A. Dias, S.C.L. Dias, *Microporous Mesoporous Mater.* 109 (2008) 485–493.

[50] B. Liu, L. France, C. Wu, Z. Jiang, V.L. Kuznetsov, H.A. Al-Megren, M. Al-Kinany, S.A. Aldrees, T. Xiao, P.P. Edwards, *Chem. Sci.* 6 (2015) 5152–5163.

[51] U. Olsbye, S. Svelle, M. Bjrgen, P. Beato, T.V.W. Janssens, F. Joensen, S. Bordiga, K.P. Lillerud, *Angew. Chem. Int. Ed.* 51 (2012) 5810–5831.

[52] A. Veses, B. Puértolas, M.S. Callén, T. García, *Microporous Mesoporous Mater.* 209 (2015) 189–196.

[53] V. Abdelsayed, D. Shekhawat, M.W. Smith, *Fuel* 139 (2015) 401–410.

[54] Y. Furumoto, Y. Harada, N. Tsunoji, A. Takahashi, T. Fujitani, Y. Ide, M. Sadakane, T. Sano, *Appl. Catal. A Gen.* 399 (2011) 262–267.

[55] N. Kumar, R. Byggningsbacka, L.-E. Lindfors, *React. Kinet. Catal. Lett.* 61 (1997) 297–305.

[56] Z. Wei, T. Xia, M. Liu, Q. Cao, Y. Xu, K. Zhu, X. Zhu, *Front. Chem. Sci. Eng.* 9 (2015) 450–460.

[57] M. Bjrgen, U. Olsbye, D. Petersen, S. Kolboe, *J. Catal.* 221 (2004) 1–10.

[58] J. Kim, M. Choi, R. Ryoo, *J. Catal.* 269 (2010) 219–228.

[59] A.A. Rownaghi, F. Rezaei, M. Stante, J. Hedlund, *Appl. Catal. B Environ.* 119–120 (2012) 56–61.